Composites Part B 176 (2019) 107111

Contents lists available at ScienceDirect

Composites Part B

journal homepage: www.elsevier.com/locate/compositesb

Variations in the distribution of local strain energy within different realizations of a representative volume element

F. López Jiménez

Ann & H.J. Smead Department of Aerospace Engineering Sciences, University of Colorado Boulder, CO, 80309, USA

ARTICLE INFO

Keywords:
Micromechanics
Finite element analysis (FEA)
Statistical properties/methods
Soft composites
Representative volume element (RVE)
Random microstructure

ABSTRACT

Numerical simulations are used to study the variations in microscopic fields between different random realizations of representative volume elements (RVE) with the same macroscopic properties. We focus on the strain energy of the matrix in unidirectional fiber composites with Neo-Hookean components, considering linear and non-linear applied loading. The simulations show significant variations in the strain energy between different realizations of the RVEs, particularly for the regions of high strain and stress concentrations that often govern damage and failure initiation. Results show a strong dependence on the volume fraction, minimum fiber distance and RVE size, as well as poor correlation between the local and the global response, which is characterized using the homogenized stiffness. In the case of non-linear loading, the rearrangement of the microstructure results in even lower correlation with the macroscopic response, as well as very strong variations according to the loading direction. We also show very poor correlation between the response in the linear and non-linear regimes for the same RVE.

1. Introduction

Fiber-reinforced composites are used as structural elements in an increasingly wide range of industrial applications, due to their excellent mechanical properties and relatively low density [1]. In recent years, increasing attention has been paid to new soft and flexible composites that exploit the effects of deformation in the geometrically nonlinear regime. Examples of this trend include fiber-reinforced elastomer composites for strain sensing [2] and deployable structures [3], soft composites made with polymeric fibers [4], and fiber reinforced hydrogel for biomedical applications [5]. While traditional composites can be analyzed assuming small deformations and linear material response on each of their components, the mechanics of this new set of composites is characterized by large deformations, material nonlinearities, and significant rearrangement of the microstructure due to loading. As such, their accurate modeling requires the development of new tools able to address their specific micromechanics.

An example of such tools are homogenization techniques for fiber composites in the nonlinear regime [6]. Following the pioneering work of Ponte Castañeda [7], several studies have provided different estimates for the nonlinear behavior of fiber-composites [8–12]. Despite significant progress in the field, the homogenization schemes proposed are fairly complex, and often require being solved numerically; closed form solutions only exist for a limited set of constituents and microstructure geometries. The process becomes even more complicated when trying to capture typical mechanisms leading to failure in composites (plasticity, fracture, fiber-matrix debonding) which depend on the local strain and stress fields within the material. Although some homogenization studies for fiber composites considering such effects exist [13], the most common approach is to use numerical homogenization.

Numerical-based homogenization [14] has been widely used in the study of both linear and nonlinear composites [15–18]. The basis of this approach is the existence of a representative volume element (RVE) with the same macroscopic response as the real material. This separation of scales between the microscopic and macroscopic scales is only strictly true in the case in which the size of the RVE is mathematically infinite, that is, extremely large compared to the characteristic lengthscale of the microstructure (*e.g.*, the fiber diameter). In order to reduce computational costs, a key step in numerical homogenization is establishing the minimum model size that provides sufficiently accurate preditions of the response of the ideal composite, as well as providing bounds for the associated error [19]. Although estimates exist in the case of composites with linearly elastic properties [20–23], in the case of nonlinear composites the critical size of the RVE depends not only on the source of nonlinearity, but also on the criteria used to establish if the model is

E-mail address: francisco.lopezjimenez@colorado.edu.

https://doi.org/10.1016/j.compositesb.2019.107111
Received 12 April 2019; Received in revised form 4 June 2019; Accepted 4 July 2019
Available online 9 July 2019

truly representative of the behavior of the infinite composite. While several studies have focused on the convergence of the homogenized mechanical response (*e.g.*, the macroscopic average stiffness), as the model size increases [24–30], comparatively little attention has been paid to the effect of RVE size on the local fields.

One of the main advantages of numerical-based homogenization is the possibility to readily access local stress and strain fields. This allows, for example, direct comparison of finite element predictions and experimental results obtained with digital image correlation at the microscopic scale [31,32]. Furthermore, it makes it possible to model failure processes using criteria based on local fields, such as fracture and cracking [33,34], plasticity [35], softening [36] and fiber-matrix debonding [37,38]. These analysis are extremely sensitive to the existence of stress concentrations due to clustering of the inclusions, which often have a much smaller effect on the homogenized response, as previously studied in several heterogeneous sytems [39–41]. As such, guidelines for the size of RVE obtained using macroscopic properties are usually not valid, and most studies perform independent convergence studies considering their specific failure mechanism, which is numerically costly. In an attempt to provide insight that is independent of the specific source of damage or failure, some studies have directly focused on the relationship between microstructure and local fields, showing how the parameters of the RVE, such as size and fiber volume fraction, determine the variations in maximum stress, or its distribution within the matrix, for different random realizations of the same RVE [42–44].

Here, we follow the same philosophy, using multiple sets of 200 nominally identical RVEs each, to investigate the influence of different parameters on the response at the microscopic scale, including RVE size, volume fraction, minimum distance between fibers and loading direction. As an important difference with results found in literature, we consider both linear and non-linear loading, where the large deformations results in severe re-arrangement of the microstructure, leading to more pronounced variations of the microscopic response. In addition, instead of focusing on the maximum stress, which might not only be extremely local, but also depend on mesh size, the results will show the local strain energy corresponding to different percentiles of its distribution within the model. Finally, we also study the correlation between the macroscopic and microscopic response for each of the RVEs analyzed.

The numerical model used in this study will be detailed in Section 2, including some background on the homogenization theory used to normalize the results. The results will be then presented in Section 3, starting with a general overview of the method used to process the simulations, followed by parametric studies considering RVE size, minimum separation between fibers and loading orientation. The manuscript concludes with a summary of the main findings and a discussion of their significance in Section 4.

2. Computational model

The composite material is idealized as an isotropic matrix reinforced with perfectly parallel cylindrical fibers, modeled using the commercial finite element package Abaqus. The RVEs are loaded applying a macroscopic deformation gradient $\overline{\mathbf{F}}$ through a combination of dummy nodes and periodic boundary conditions, which is equal to the average of the local deformation gradient [45]:

$$\overline{\mathbf{F}} = \frac{1}{V}\int_V \mathbf{F}(\mathbf{X}) d\mathbf{X} \,, \tag{1}$$

where V is the volume of the RVE and $\mathbf{F} = \partial \mathbf{x}/\partial \mathbf{X}$ is the local deformation gradient. Throughout the manuscript the same convention will be used to distinguish between local, A, and homogenized (*i.e.* global), $\overline{A}$, versions of any given field, A. As such, A will depend on the position within the RVE, while $\overline{A}$ has been obtained through numerical homogenization and is unique for the whole model. In addition, $\tilde{A}$ will refer to predictions of macroscopic properties obtained with homogenization theory, see Section 2.3.

2.1. Geometry and fiber arrangement

The composite is idealized as a matrix reinforced by cylindrical fibers of radius r, extending perfectly parallel in the X_1 direction and with a random distribution within the $X_2 - X_3$ plane. The composite is therefore transversely isotropic, *i.e.* isotropic in the plane perpendicular to the fiber direction. The fiber volume fraction is V_f. In the simulations presented here we assume plane strain to reduce the geometry to a square two-dimensional RVE of side length $L_2 = L_3 = L = \delta r$, with $N_f = V_f \delta^2/\pi$ fibers. Assuming generalized plane strain yields identical results, since the stiffness of the fibers with respect to the matrix prevents any stretching in the X_1 direction. A schematic of the model, as well as an example of a loaded RVE, is shown in Fig. 1.

For a given model size, δ, and fiber concentration, V_f, the microstructure is fully described by the position of the center of the fibers within the RVE. These are obtained through a random sequential adsorption algorithm [46]. This is a hard-core process, *i.e.* a Poisson process in which a limitation on the minimum distance between the centers is introduced: the positions of the fibers are obtained randomly, and rejected if the distance to any of the already existing fibers is less than a prescribed limit. In this work, and unless noted otherwise, the minimum distance adopted is 1.1 times the diameter. Additionally, a fiber is also rejected if the distance between its center to the edge of the RVE is in the $[0.9r,\ 1.1r]$ interval. The goal of both conditions is creating a geometry that can be easily meshed. An average element size of $0.1r$ has been chosen after a parametric mesh size study. A possible outcome of the method is a jammed configuration [47], in which no new fibers can be added without violating the non-overlap restriction. For this reason, if after 1000 attempts a new fiber has not been accepted, the microstructure is discarded and the algorithm starts from zero. In the case of the present study, and taking into account the extra distance

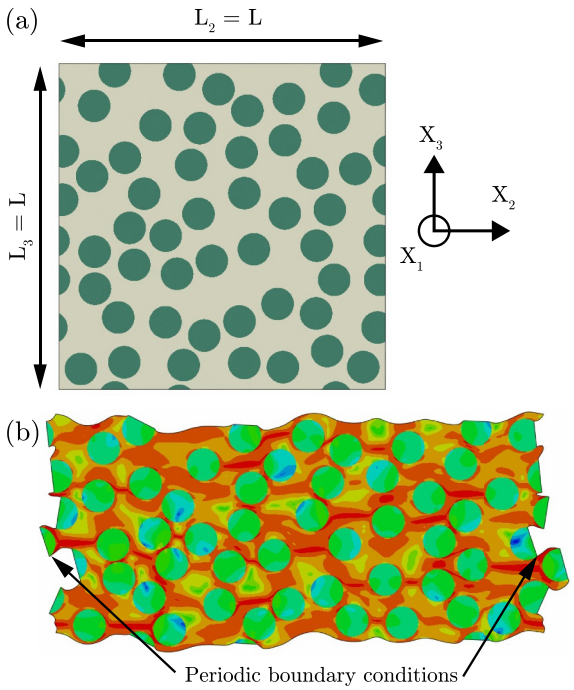

Fig. 1. Representative volume element (RVE) in the underformed (a) and deformed configurations (b). The example has $V_f = 0.4$ and $\delta = 20$, and it has been stretched by $\lambda = 1.5$ in the x_2 direction. The color represents the strain energy density. (For interpretation of the references to color in this figure legend, the reader is referred to the Web version of this article.)

between fibers to facilitate meshing, it is not possible to systematically create RVEs with volume fraction of 0.5 or higher. Although there are alternative methods that allow for fiber overlap, which are then corrected through modifications of the microstructure [38,43], they result in a fiber arrangement that is not completely equivalent to that produced by a pure Poisson process. In order to ensure consistency through volume fractions, we limit ourselves to the range $Vf = \{0.2, 0.3, 0.4\}$. Although lower than traditional values used for traditional epoxy based composites, this corresponds to the range of fiber reinforced soft composites that have been studied experimentally in the literature [38,48].

Several studies have focused on the characterization of the microstructure of real composites [49–51] as well as in the development of techniques able to create random microstructures that are statistically equivalent to those observed in micrographs [52–55]. Although there are studies comparing different approaches [56,57], the conclusions are dependent on the specific experimental system, as well as the mechanical phenomena of interest (*e.g.*, the specific source of failure or non-linearity). In order to provide more general results, we will limit the present study to purely random fiber arrangements. Furthermore, it has been shown that Poisson and hard-core processes (with small restrictions on the minimum fiber distance) result on microstructures with similar radial distribution function that those observed experimentally [57].

2.2. Boundary conditions and applied loading

Periodic boundary conditions are applied in all faces of the RVE using the command EQUATION in Abaqus, which requires that the pairs of opposite faces are meshed identically. The conditions can be summarized as:

$$\begin{aligned} \mathbf{u}(L_2, X_3) - \mathbf{u}(0, X_3) &= \overset{2}{\mathbf{u}} \\ \mathbf{u}(X_2, L_3) - \mathbf{u}(X_2, 0) &= \overset{3}{\mathbf{u}} \end{aligned} \tag{2}$$

where $\overset{i}{u}_j$ corresponds to the difference in displacement in the $j-$ *th* direction between pairs of nodes in the face perpendicular to the $i-$ *th* axis. In practice, the displacements $\overset{i}{\mathbf{u}}$ are those of dummy nodes (one per pair of faces) used to control their relative displacements. As an example, $\overset{2}{\mathbf{u}}$ controls the relative displacements of nodes in the faces perpendicular to the X_2 axis: $\overset{2}{u}_2 > 0$ would result in an increase in distance between the nodes with coordinates $X_2 = L_2$ and $X_2 = 0$, *i.e.* expansion in the X_2 direction. The displacement $\overset{2}{u}_3$ controls shearing. In a large deformation setting, these displacements are given by $\overset{i}{u}_j = \overline{F}_{ij} L_j$, where, L_j is the length of the RVE in the j-th direction, and $\overline{\mathbf{F}}$ is the desired average deformation gradient. This way all the displacements of the dummy nodes, and therefore the relationship leading to periodicity in the boundary, are determined by $\overline{\mathbf{F}}$.

The only deformations considered in the present study will be pure stretching in the X_2 and X_3 directions, and so the deformation gradient can be expressed as a function of a single stretch λ as:

$$\overline{\mathbf{F}} = \begin{bmatrix} 1 & 0 & 0 \\ 0 & \lambda & 0 \\ 0 & 0 & \dfrac{1}{\lambda} \end{bmatrix}, \tag{3}$$

which verifies both the conditions for plain strain, $\lambda_1 = 1$, and incompressibility, $\lambda_1\lambda_2\lambda_3 = 1$. The principal stretches in the plane are then λ, in the X_2 direction, and $1/\lambda$, in the X_3 direction. It should be noted that, due to incompressibility, all deformations are equivalent to pure shear.

As explained before, the components of $\overset{i}{\mathbf{u}}$ can be obtained directly from the desired macroscopic deformation, and imposed to the model through the auxiliary dummy nodes. However, imposing the four displacements can lead to numerical errors: even small rounding errors on the applied relative displacement of the boundary nodes might result in a net change in RVE area, which no matter how small represents a violation of the incompressibility condition. In practice, this is resolved by allowing free expansion in the X_3 direction, meaning that $\overset{3}{u}_3$ is not imposed. The displacement of the dummy node is then tracked during the simulations, to confirm that $\overset{3}{u}_3 = F_{33} L_3$ as expected.

2.3. Material properties

Fibers and matrix are modeled as incompressible hyperelastic Neo-Hookean materials, with strain energy density defined as

$$W_i = \mu_i / 2 (I_1 - 3), \tag{4}$$

where μ_i is the linear shear stiffness of the $i-$ *th* component (*f* for fiber, *m* for matrix), and I_1 is the first invariant of the Cauchy-Green deformation tensor $\mathbf{C} = \mathbf{F}^\intercal\mathbf{F}$, which can be defined as a function of the principal stretches λ_i as $I_1 = \sum_{i=1}^{3} \lambda_i^2$ [58]. The bonding between both components is assumed to be perfect. The ratio of stiffness between fibers and matrix is $\mu_f/\mu_m = 10000$, which has been shown to be equivalent to assuming the fibers to be rigid [59]. Both components are modeled with linear quadrilateral elements CPE4H, with hybrid formulation to account for incompressibility.

The response of an unidirectional fiber composite with Neo-Hookean components can be approximated by the homogenized response:

$$\tilde{W} = \frac{\tilde{\mu}_{IH}}{2}(\overline{I}_1 - 3) + \frac{\tilde{\mu}_n - \tilde{\mu}_{IH}}{2}\left(\frac{2}{\sqrt{\overline{I}_4}} - 3\right) + \frac{\tilde{\mu}_n - \tilde{\mu}_{HS}}{2}\overline{I}_4 - \frac{\tilde{\mu}_{IH} - \tilde{\mu}_{HS}}{2}\frac{\overline{I}_5}{\overline{I}_4} \tag{5}$$

where

$$\begin{aligned} \tilde{\mu}_{IH} = {} & (1 - V_f)^2 \left(1 + \frac{2(2 - V_f)V_f}{(1 - V_f)^2}\frac{\mu_f}{\mu_m} + \frac{\mu_f^2}{\mu_m^2}\right)\frac{\mu_m}{2} \\ & - (1 - V_f)^2 \sqrt{\frac{2}{(1 - V_f)^2}\frac{\mu_f}{\mu_m} + \left(1 + \frac{2(2 - V_f)V_f}{(1 - V_f)^2}\frac{\mu_f}{\mu_m} + \frac{\mu_f^2}{\mu_m^2}\right)}\frac{\mu_f - \mu_m}{2} \end{aligned} \tag{6}$$

$$\tilde{\mu}_{HS} = \frac{(1 - V_f)\mu_m + (1 + V_f)\mu_f}{(1 + V_f)\mu_m + (1 - V_f)\mu_f}\mu_m \tag{7}$$

In this case $\overline{I}_i$ are the invariants of the homogenized Cauchy-Green deformation, obtained from the average deformation tensor, $\overline{\mathbf{C}} = \overline{\mathbf{F}}^\intercal\overline{\mathbf{F}}$. The fourth and fifth invariants are defined as:

$$\overline{I}_4 = \mathbf{N}^\intercal\overline{\mathbf{C}}\mathbf{N} \tag{8}$$

$$\overline{I}_5 = \mathbf{N}^\intercal\overline{\mathbf{C}}\,\overline{\mathbf{C}}\mathbf{N}, \tag{9}$$

where $\mathbf{N} = [1\ 0\ 0]^\mathrm{T}$ is the unit vector in the fiber direction. The fourth invariant $\overline{I}_4$ represents stretch in the fiber direction. The fifth invariant $\overline{I}_5$ does not have a direct physical interpretation, but $\overline{I}_5 = 1$ for deformation in the plane perpendicular to the fiber direction, and so it helps differentiate between in-plane and out-of-plane deformations.

Equation (5) combines homogenization predictions obtained using two different schemes: $\tilde{\mu}_{IH}$ is a result of second order iterative homogenization [60], while $\tilde{\mu}_{HS}$ is based on solutions for coated laminates [8,9,12] and coincides with the Hashin-Shtrikman lower bound. Although the derivation assumes a polydisperse fibers, it has been hypothesized that the prediction serves as a lower bound for monodisperse composites such as those considered here [11]. Equation (5) has been shown to

agree with results from numerical homogenization in RVEs of unidirectional hyperelastic monodisperse composites under general loading [59]. In the case of plane strain in the $X_2 - X_3$ plane there is no deformation corresponding to the fourth and fifth invariants, $\bar{I}_4 = \bar{I}_5 = 1$, and Equation (5) reduces to:

$$\tilde{W}(\bar{I}_4 = \bar{I}_5 = 1) = \frac{\tilde{\mu}_{IH}}{2}(\bar{I}_1 - 3)\,, \tag{10}$$

which is the prediction obtained though iterative homogenization, and which will be used to normalize the results in this study.

3. Results

In order to present the results in a non-dimensional form, we will use the homogenization prediction in Equation (10). Although it is an estimate for the strain energy density of the complete composite, the contribution of the fibers is found to be several orders of magnitude lower than that of the matrix, regardless of the fiber volume fraction. The total strain energy is then basically equal to the strain energy in the matrix, and so the strain energy density of the matrix can then be approximated by that of the composite, corrected to account for only the volume of the matrix:

$$\tilde{W}_m \approx \frac{\tilde{W}}{1 - V_f} \tag{11}$$

For the rest of the study, we will refer to the non-dimensional strain energy as $\widehat{W}$:

$$\widehat{W} = \frac{W}{\tilde{W}_m}\,, \tag{12}$$

where it is implicitly assumed that $\tilde{W}_m$ is defined using the appropriate fiber concentration, V_f. Following our naming convention, $\tilde{W}_m$ is a prediction obtained through homogenization theory, and W is the strain energy local field, which depends on the position within the RVE; therefore, $\widehat{W}$ is also a local field, $\widehat{W} = \widehat{W}(\mathbf{X})$ (in practice, there is a value of W and $\widehat{W}$ associated to each matrix element of the RVE).

We will also use the homogenized shear stiffness, $\bar{\mu}$, to characterize the global response of the RVE. Assuming that the response of the RVE can be approximated as a Neo-Hookean material [38], it can be calculated from the homogenized strain energy density $\overline{W}$ as:

$$\bar{\mu} = \frac{2\overline{W}}{\bar{I}_1 - 3}\,, \tag{13}$$

which will be normalized by the value predicted by the homogenization theory, $\tilde{\mu}_{IH}$ in Equation (6).

The homogenized strain energy density $\overline{W}$ is calculated as:

$$\overline{W} = \frac{\int_A W dA}{A} = \frac{\int_{A_f} W_f dA_f + \int_{A_m} W_m dA_m}{A_f + A_m}\,, \tag{14}$$

where the integral has been evaluated separately in the two phases: W_i and A_i are the strain energy density and area of either fiber, f, or matrix, m. The integral can be calculated numerically from the simulations, by simply adding the energy of all matrix and fiber elements. As mentioned before, the contribution of the matrix (W_m) is several orders of magnitude higher than that of the fibers (W_f).

It should be noted that the values of L used in the study are not exactly equal to δr. Instead, the simulations use the closest value giving an integer number of fibers, so that the fiber volume fraction is strictly enforced. Table 1 summarizes the number of fibers on each of the geometries considered; 200 different realizations of the RVE have been created for each combination of V_f and δ.

Table 1
Number of fibers and final RVE size for the values of δ and V_f considered in the study.

		V_f			
		0.1	0.2	0.3	0.4
δ	10	$N_f = 3$ $L = 9.71\,r$	$N_f = 6$ $L = 9.71\,r$	$N_f = 10$ $L = 10.23\,r$	$N_f = 13$ $L = 10.10\,r$
	20	$N_f = 13$ $L = 20.20\,r$	$N_f = 25$ $L = 19.82\,r$	$N_f = 38$ $L = 19.95\,r$	$N_f = 51$ $L = 20.01\,r$
	30	$N_f = 29$ $L = 30.18\,r$	$N_f = 51$ $L = 29.92\,r$	$N_f = 86$ $L = 30.01\,r$	$N_f = 115$ $L = 30.05\,r$
	40	$N_f = 51$ $L = 40.03\,r$	$N_f = 102$ $L = 40.03\,r$	$N_f = 153$ $L = 40.03\,r$	$N_f = 204$ $L = 40.03\,r$

3.1. Example of results

The present study focuses on the strain energy density of the matrix, which has been calculated as the total strain energy of each element divided by its area. In order to limit the influence of the mesh size, we will avoid focusing on the maximum strain energy at a given element. Instead, we will use the procedure detailed in the following example. It corresponds to the case of $V_f = 0.3$ and $\delta = 20$, and it has been applied to all the other cases considered in this study.

For each simulation, we can calculate the fraction of matrix area in which the strain energy is higher than a given threshold $\widehat{W}^*$:

$$\widehat{A}_{\widehat{W}}(\widehat{W}^*) = \frac{\sum_{\widehat{W}_i > \widehat{W}^*} A_i}{A_m}\,, \tag{15}$$

where A_i and $\widehat{W}_i$ are the area and non-dimensional strain energy density of the i-th element of the matrix, and A_m is the total area of the matrix, $A_m = \sum_i A_i$. In pratice, this is done by adding the area of all matrix elements with strain energy higher than $\widehat{W}_i$, and dividing it by the total matrix area.

Fig. 2 (a) shows the evolution of $\widehat{A}_{\widehat{W}^*}$ for the 200 different realizations of the RVE with $V_f = 0.3$, $\delta = 20$ and an applied stretch $\lambda = 1.01$, with one specific realization highlighted. As expected, $\widehat{A}_{\widehat{W}}(\widehat{W}^* = 0) = 1$, since the whole matrix has at least zero strain energy, and it decreases as $\widehat{W}^*$ increases. All curves are smooth at first, but take discrete steps for very low values of $\widehat{A}_{\widehat{W}}$. The reason is that for very high values of $\widehat{W}^*$ only a few elements contribute to the sum in Equation (15). In this study we will only consider $\widehat{A}_{\widehat{W}} \geq 10^{-3}$, so that we can still assume that the simulations behave like a continuum.

We then consider the three horizontal lines in Fig. 2(a), corresponding to $\widehat{A}_{\widehat{W}} = \{0.1, 0.01, 0.001\}$, that is, the 10%, 1% and 0.1% of elements with highest strain energy. These thresholds in matrix area allow us to define a given strain energy level for each RVE, $\widehat{W}^*_p$, defined as the strain energy for which:

$$\widehat{A}_{\widehat{W}}\left(\widehat{W}^*_p\right) = p \tag{16}$$

As such, the p-fraction of the matrix with highest strain energy has at least an energy equal to $\widehat{W}^*_p$. Smaller values of p correspond to increasingly small fractions of the matrix area, and therefore increasingly larger values of the local strain energy of the matrix ($\widehat{W}^*_p < \widehat{W}^*_q$ for all $p > q$). During the text, we will use either $\widehat{W}^*_p$ or $\widehat{A}_{\widehat{W}} = p$ to identify the results.

It is clear from Fig. 2(a) that different realizations of the same RVE have very different values of $\widehat{W}^*_p$, particularly for small values of p, since

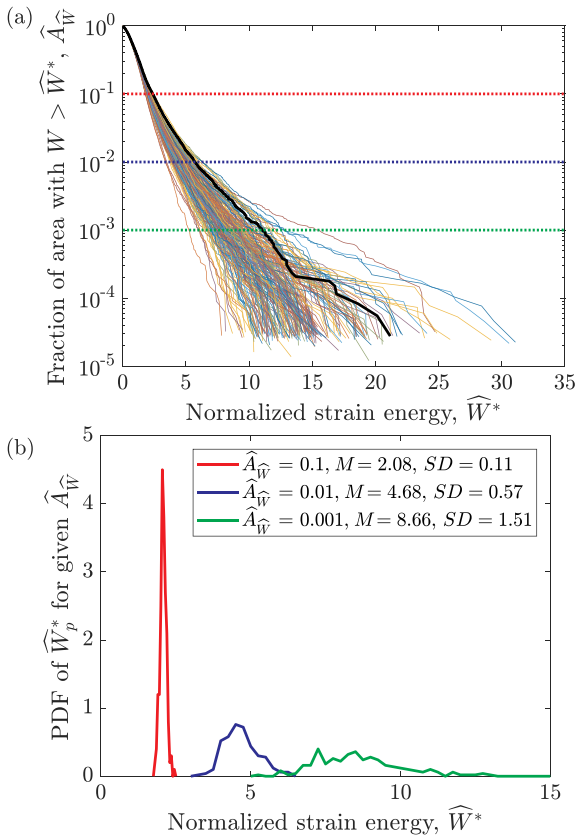

Fig. 2. Example of the analysis procedure: (a) Fraction of area with strain energy higher than the threshold $\widehat{A}_{\widehat{W}}$, for 200 different RVEs, with one of them highlighted as a bold black line. All RVEs have $\delta = 20$ and $V_f = 0.3$, and the applied deformation is $\lambda = 1.01$. (b) Histogram of the threshold strain $\widehat{W}_p^*$ for all 200 different RVEs and $p = \{0.1,\ 0.01,\ 0.001\}$. The legend lists the mean (M) and standard deviation (SD) of each distribution.

those correspond to regions with high strain and stress concentrations within the fibers, where the dependence on the microstructure is more pronounced. Fig. 2(b) shows the histograms of all the three values of $\widehat{W}_p^*$ considered ($p = \{0.1, 0.01, 0.001\}$), for the 200 realizations of the RVE. In other words, the red line in Fig. 2(b) shows the distribution of the *lowest* strain energy out of all the matrix elements that belong to the 10% of the matrix with the *highest* strain energy. The results show that for $p = 0.1$ there is little variation between different RVEs, while the high values associated with $p = 0.01$ and $p = 0.001$ have increasingly larger spread. The mean (M) and standard deviations (SD) of the distributions are provided in the legend.

In order to further illustrate the meaning of the parameters chosen to present the results, Fig. 3 shows the strain energy of the RVE highlighted in Fig. 2(a), with the scale in the color representing different values of p, including the main values used in the study, $p = \{0.1, 0.01, 0.001\}$. In Fig. 3(b–e) the scale is binary, with the green color corresponding to energies below $\widehat{W}_p^*$, with $p = \{0.75, 0.5, 0.25, 0.1\}$, and red for higher energies. The sequence shows how, as p decreases, the area with high strain energy is mostly relegated to regions between closely packed fibers, as expected. The present study has focused on strain energy for conciseness, but plotting other quantities, such as a maximum principal strain, reveals very similar contour plots, indicating that both quantities are highly correlated, as expected.

3.2. Effect of model size and fiber volume fraction

We first explore the effect of the RVE size, δ, and the fiber volume

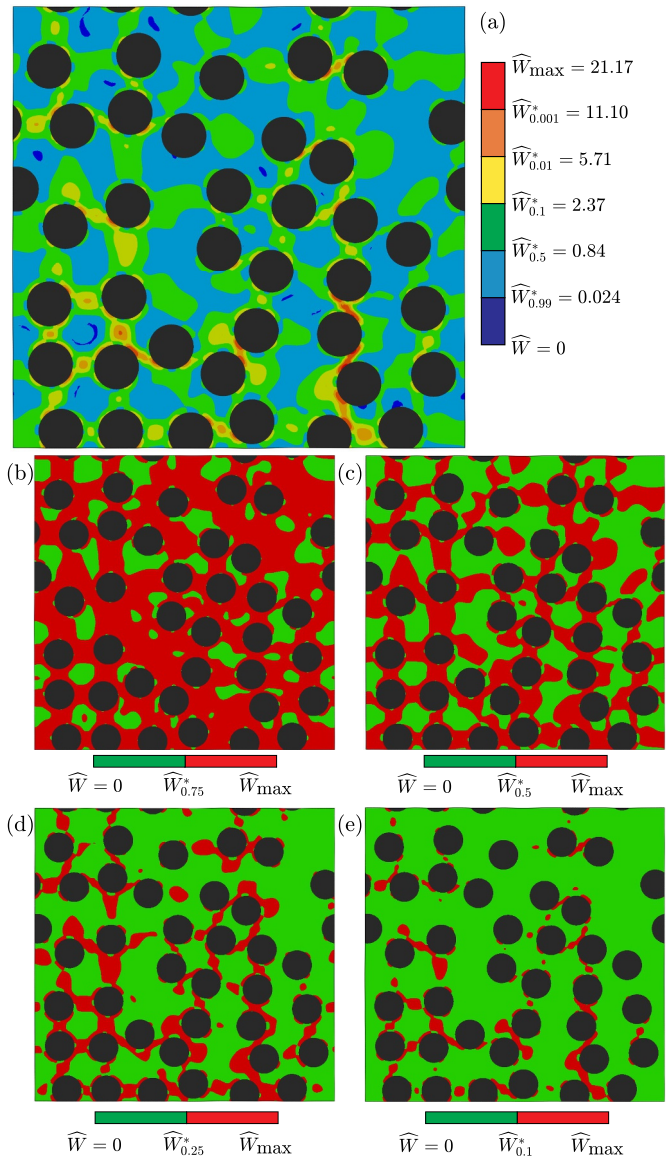

Fig. 3. Colour contours of the strain energy in the matrix of the RVE highlighted in Fig. 2(a), for different values of $\widehat{W}_p^*$ (a), as well as the same RVE with difference binary scales for the color bar, showing the reduction in area as p decreases (b–e), with the regions of high local strain energy located between closely packed fibers. The model has $V_f = 0.3$ and $\delta = 20$, and the applied loading is $\lambda = 1.01$. (For interpretation of the references to color in this figure legend, the reader is referred to the Web version of this article.)

fraction, V_f. Previous studies have shown that for $\delta \geq 30$ there is very small variation in the macroscopic response within different realizations of a given RVE [61]. Our goal is to explore if the same can be said about the local variations in strain energy, since these will be important to model nonlinear effects such as damage and debonding. Fig. 4 shows the probability density functions of $\widehat{W}_p^*$ for an applied stretch in the linear regime, $\lambda = 1.01$, as well as a value well into the nonlinear regime, $\lambda = 1.5$, and different values of the RVE size and fiber volume fraction. The same results are presented as mean and standard deviation ($M \pm SD$) in the Figure insets.

For $p = 0.1$, the results are very similar in all cases: the average values are very similar regardless of the fiber concentration, roughly 2 to 2.5 times higher than the values predicted by homogenization theory, and the standard deviations are very small regardless of the values of δ and V_f. As the value of p increases, two effects can be observed. First, a

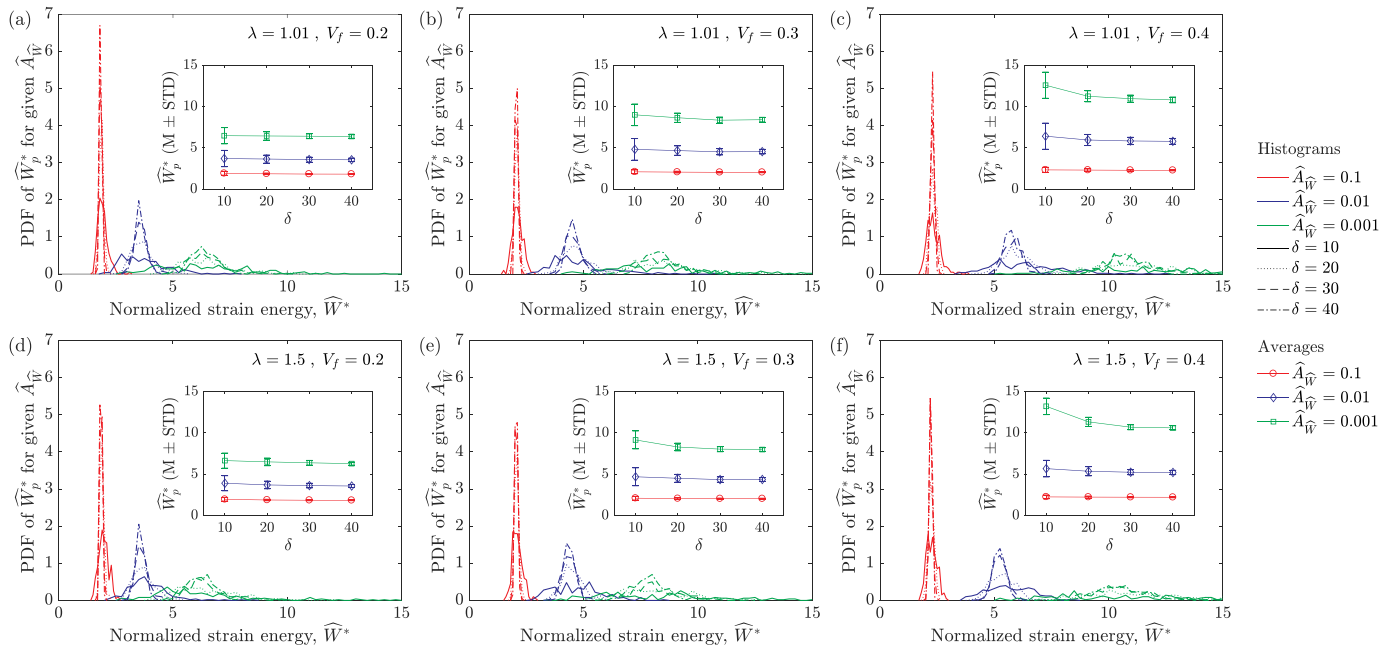

Fig. 4. Probability density function of the distribution of $\widehat{W}_p^*$ for $p = 0.1, 0.01, 0.001$ and different values of the RVE size, δ, and fiber volume fraction, V_f. The applied stretch is $\lambda = 1.01$ (a–c) and $\lambda = 1.5$ (d–f). The insets show the same results expressed as mean and standard deviation ($M \pm SD$), as a function of the RVE size, δ.

pronounced dependence on the volume fraction: the values of $\widehat{W}_{0.001}^*$ are roughly twice for the most dense RVEs considered ($V_f = 0.4$) than for the most dilute ($V_f = 0.2$). Second, the convergence with the RVE size (δ) changes, and it also shows a relationship with the volume fraction. For dense systems, $V_f = 0.4$, convergence for the case of $p = 0.001$ is only achieved for $\delta \geq 30$.

In all cases of the small RVEs, $\delta = 10$, the distributions also show large values of the standard deviation, specially in the case of dense systems: in models with a small number of fibers it is more likely that a significant portion of them are very closely packed, while as the size of the model increases, the fiber distribution within a given realization of the RVE tends to be more homogeneous (*i.e.*, a small cluster of fibers will have a relatively smaller effect).

Remarkably, the results are very similar for loading in the linear regime, $\lambda = 1.01$, and the non-linear regime, $\lambda = 1.5$, both in terms of the values of $\widehat{W}_p^*$, as well as their dependence with respect to the RVE parameters, δ and V_f.

3.3. Effect of fiber distance

As detailed in Section 2.1, a key parameter in the creation of the RVEs is the imposed minimum distance between fibers, d. In practice, the value of d is often chosen to ensure a proper meshing of the model, but it does affect the physics of the problem. Small values of d allow the appearance of clusters of tightly packed fibers, while relatively large values of d result in RVEs with a more homogeneous distribution of the fibers, and therefore less likely to have high stress and strain concentrations. In order to quantify this effect, Fig. 5 show results with simulations with $V_f = 0.3$ and minimum fiber distances $d/(2r) = \{1.05, 1.1, 1.15\}$, again for both the linear and non-linear regime.

The results show that the minimum fiber distance has very little effect on the strain energies at the $\widehat{W}_{0.1}^*$ level, at least for the range of d considered. The effect is much more pronounced for higher values of the strain energy, particularly for $p = 0.001$, even for the largest value of δ considered. As before, the results are very similar for the linear ($\lambda =$

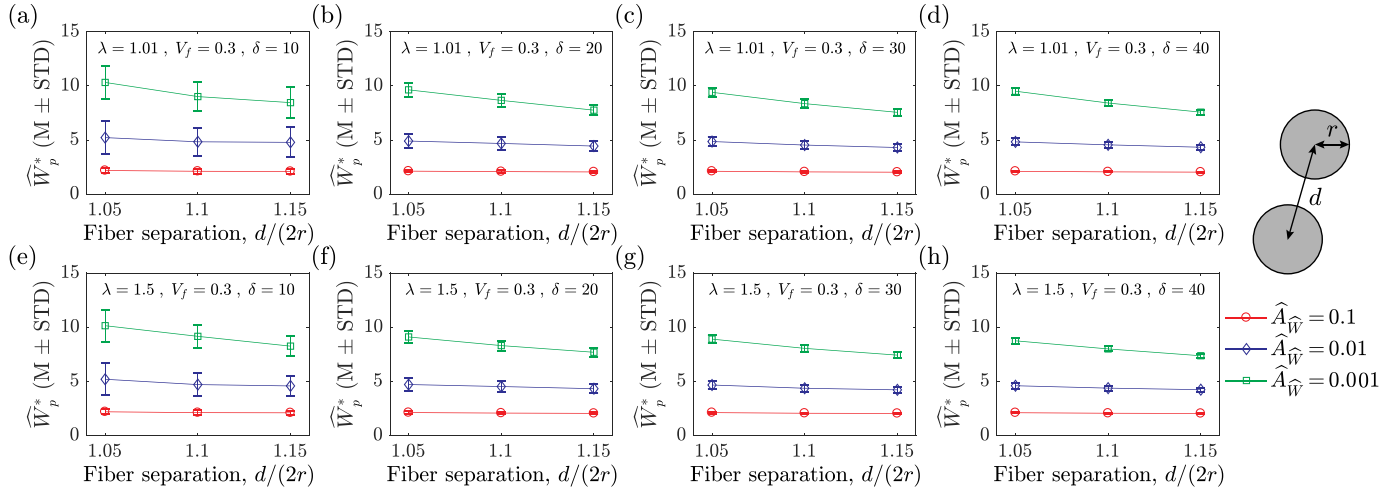

Fig. 5. Mean and standard deviation of the distribution of $\widehat{W}_p^*$ for $p = \{0.1, 0.01, 0.001\}$ and different values of the RVE size, δ and minimum fiber distance, d. The fiber volume fraction is $V_f = 0.3$, and the applied stretch is $\lambda = 1.01$ (a–d) and $\lambda = 1.5$ (e–h).

1.01) and non-linear regimes ($\lambda = 1.5$).

3.4. Correlation between linear and non-linear regimes

The previous results have shown similar global trends when the RVEs are loaded in the linear and non-linear regimes. We now investigate the possibility of a direct correlation between the two, that is, if a RVE with particularly high strain and stress concentrations in the linear regime will also have high values of the strain energy when the applied stretch is increased to the non-linear regime. Such a relationship could be used to reduce computational cost, by identifying RVEs of interest with simulations in the linear regime, before performing a geometrically non-linear analysis.

Fig. 6(a and b) plots the energy levels for $\widehat{W}_p^*$ for the same RVEs in the linear versus the non-linear regime, plus the best linear fit. The R^2 values are given on each figure, as a way to indicate the quality of the fit. The values of p and V_f correspond to the two most extreme cases: the highest R^2 value ($p = 0.1$ and $V_f = 0.2$), in which the correlation is already weak ($R^2 = 0.6$), as well as the lowest ($p = 0.001$ and $V_f = 0.3$), in which there is basically no correlation ($R^2 = 0.23$). Fig. 6(c) shows the trend more clearly, by plotting the R^2 of the fit between parameters in the linear and non-linear regime: macroscopic stiffness, obtained through numerical homogenization, and normalized by analytical predictions, $\overline{\mu}/\tilde{\mu}_{IH}$, and the energy levels $\widehat{W}_p^*$, as a function of the volume fraction V_f. It should be mentioned that the values of R^2 used in the plot have been obtained with a fit using all values of δ. In order to identify possible effects of the RVE size, the error bars have been calculated using the standard deviation between the R^2 values of five different options to calculate the fit: using all RVE sizes, as well as each of the four values of δ independently. The relatively small value of the error bars indicates that the results are not an artifact of the size of the RVE.

As indicated before, the correlation values range from poor to very low. They are highest (R^2 in the 0.5 to 0.7 range) for the homogenized stiffness, and lower for $\widehat{W}_{0.1}^*$ and $\widehat{W}_{0.01}^*$ (R^2 in the 0.65 to 0.35 range, indicating no meaningful correlation). The values of R^2 are even lower for the highest energy level considered, $p = 0.001$. There is also a strong dependence on the fiber volume fraction, with all values of R^2 decreasing as V_f increases, indicating that the fiber arrangements associated with dense packing of fibers are more likely to be drastically rearranged due to large applied stretches, resulting in a radically different behavior between the linear and non-linear regimes. Overall, Fig. 6(c) shows that there is a very weak correlation between the two regimes, and so the results from a linear analysis do not provide information about the expected response under non-linear deformation, particularly for dense systems.

3.5. Correlation with macroscopic stiffness

Another interesting correlation to explore is that of local strain energy levels within the matrix, and the macroscopic response, defined by the homogeneous stiffness $\overline{\mu}/\tilde{\mu}_{IH}$. Since almost all the strain energy in the system is contributed by the matrix, and the stiffness is directly determined by the energy of the system, there is an obvious relationship between the stiffness and the *total* strain energy of the matrix. However, it is not clear if the same relationship takes place when higher levels of the strain energy (*i.e.*, only regions with high strain and stress concentrations) are considered.

Fig. 7 shows the quality of a linear fit between homogenized sitffness, $\overline{\mu}/\tilde{\mu}_{IH}$, and all three energy levels considered, $\widehat{W}_p^*$ for $p = \{0.1, 0.01, 0.001\}$, as a function of the fiber volume fraction and the applied stretch. The procedure to determine values and error bars is the same as in Fig. 6 (c). The results show that there is a significant relationship between the macroscopic response and the local strain energy for energy levels with

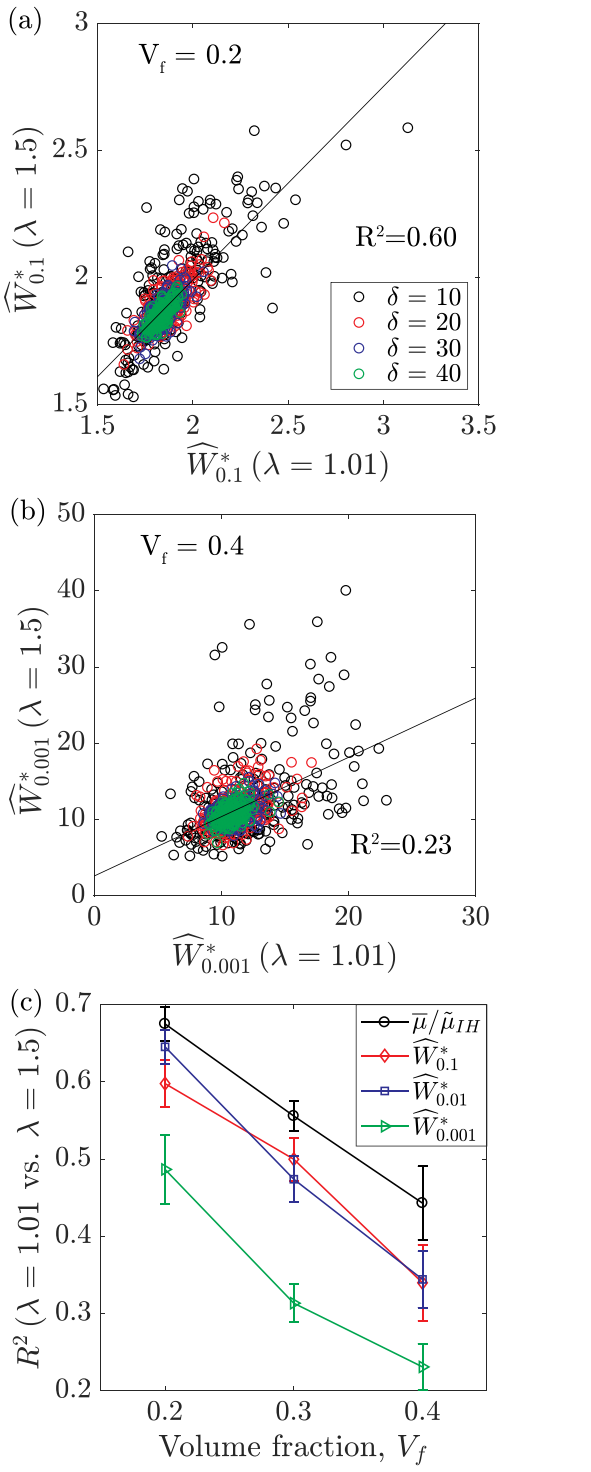

Fig. 6. Correlation of local strain energy density levels, $\widehat{W}_p^*$, for linear ($\lambda = 1.01$) and non-linear ($\lambda = 1.5$) applied loads, for (a) $p = 0.1$ and $V_f = 0.2$, and (b) $p = 0.001$ and $V_f = 0.4$; the same legend applies to both. Each data point is an individual RVE, and the lines correspond to a linear fit obtained using all values of δ; the values of R^2 are displayed for each fit. (c) R^2 value for the correlation between homogenized stiffness, $\overline{\mu}$, and energy levels $\widehat{W}_p^*$, at the two different levels for applied stretch, for different values of p and V_f. The values correspond to a linear fit obtained using all values of δ. The error bars are the standard deviation between the fit considering all values of the RVE size, as well as fits using the individual values of δ.

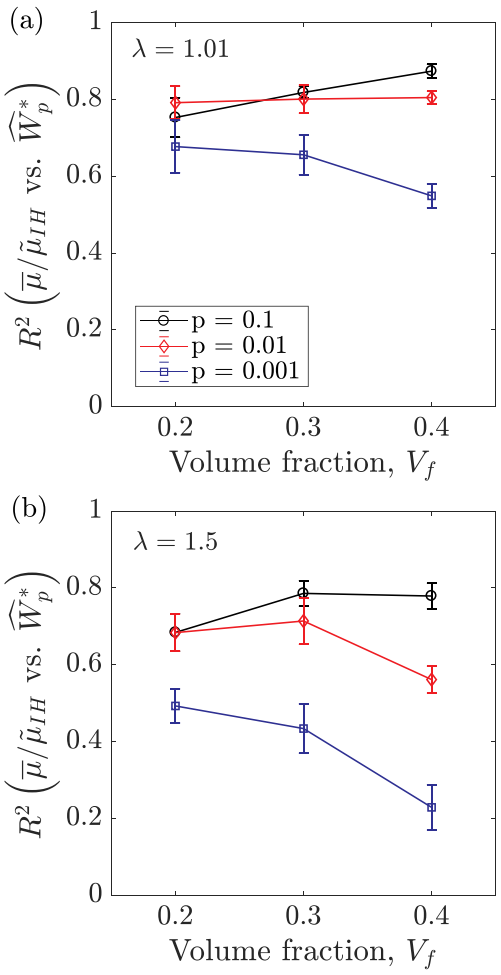

Fig. 7. value for the best linear fit between homogenized stiffness, $\overline{\mu}$ and energy levels $\widehat{W}_p^*$, for different values of p and V_f, for (a) $\lambda = 1.01$ and (b) $\lambda = 1.5$. The values correspond to a linear fit obtained using all values of δ. The error bars are the standard deviation between the fit considering all values of the RVE size, as well as fits using the individual values of δ. The legend applies to both plots.

$p \leq 0.01$ (R^2 in the 0.75 to 0.9 range), but a significantly weaker relationship for $p = 0.001$ ($R^2 \approx 0.6$), which corresponds to very high strain and stress concentrations. In all cases, the values of R^2 are lower in the nonlinear regime than for the case of small deformations.

Interestingly, the dependence on the volume fraction changes with the values of p. For $\widehat{W}_{0.1}^*$, the correlation increases with the fiber concentration, while it decreases for the case of $\widehat{W}_{0.001}^*$, particularly in the nonlinear regime. The hypothesized reason is the fact that, as the volume fraction increases, the fiber distribution is at the same time more homogeneous *in general* (meaning less likely to show large regions of pure matrix), resulting in a more homogeneous distribution of the moderate values of the strain energy, that correlates better with the *total* strain energy, and therefore with the stiffness of the RVE. In dense systems, on the other hand, it is much more likely to find RVEs with highly localized regions of very closely packed fibers, in which high strain and stress concentration do not translate into an equally high overall stiffness, explaining the poor correlation between $\overline{\mu}$ and $\widehat{W}_{0.001}^*$.

3.6. Effect of loading direction

We finally explore the effect of varying the loading direction for the same model. A study exploring the isotropy of different RVEs of unidirectional composites [61] showed that, in the linear regime, the response is approximately sinusoidal with respect to the loading direction, θ, with a half-period of $\pi/2$ radians (meaning identical response under loading in perpendicular directions). In the non-linear regime, however, there is no clear dependence with respect to θ, due to the different relative displacement of the fibers. This means that the macroscopic response of a model depends not only on the particular realization of the fiber arrangement, but also on the loading direction.

To study the effect of the loading direction on the local strain energy distribution, the RVEs with $V_f = 0.3$ have been loaded in both the X_2 and X_3 direction. Fig. 8 shows the correlation between energy levels for both loading directions, as well as the correlation between macroscopic stiffness. As expected, the results in the linear regime show almost perfect correlation ($R^2 > 0.99$) for all values of $\widehat{W}_p^*$, as well as the macroscopic stiffness. For $\lambda = 1.5$, on the other hand, there is a complete lack of correlation, with $R^2 < 0.2$ for all values of p, as well as for the macroscopic response. In both cases, the main effect of increasing the value of δ is decreasing the magnitude of the relative variations between different RVEs.

An important distinction to be made between the macroscopic ($\overline{\mu}$) and microscopic ($\widehat{W}_p^*$) responses in the non-linear regime is the differences that can be observed under different loading directions. In the case of the macroscopic stiffness, the relative variations are small, less than 10% for most RVEs with $\delta \geq 20$. In the case of the distribution of strain energy densities, the range of values is much larger, and so the differences for a given RVE and different loading directions can be very significant. For example, for $p = 0.001$ differences of over 50% are frequently observed even for the largest RVEs considered in this study, $\delta = 40$.

The main conclusion that can be drawn from Fig. 8 is the fact that variations in mechanical properties when a given RVE is loaded in two different directions are as significant as the variations between different realizations of the RVE. The results agree with a previous study that focused on the anistropy of the macroscopic response at both the linear and non-linear regimes [61]. This implies that even if RVE number 1 is stiffer than RVE number 2 when the loading is applied in the X_2 direction, the opposite could be true when the load is applied in the X_3 direction; the same applies to the stress and strain concentrations in the matrix. As such, studies trying to characterize each RVE with a single parameter (*e.g.* stiffness) describing its mechanical behavior, in order to rationalize the variations between different realizations (*e.g.*, by relating them to descriptions of the microstructure) need to take into account this anisotropy, for example by choosing a sufficiently large RVE size or averaging over different loading directions [62–64].

4. Discussion

Numerical simulations with sets of 200 nominally identical RVEs were used to investigate the relationship between different parameters used to generate the models, and their response at the microscopic scale. The strain energy of the matrix is defined by considering $\widehat{W}_p^*$, the values corresponding to the p-fraction of the matrix with highest strain energy, so that lower values of p correspond to increasingly small regions with very high stress and strain concentrations. All RVEs generated have been loaded with both linear and nonlinear applied stretches, to investigate the effect of the microstructure rearrangement associated with large applied deformations.

The results show that the energy levels for $p = 0.1$ are very similar regardless of RVE size and volume fraction, with little variation between different realizations of the same RVE. As p decreases, that is, for higher local values of the strain energy, the variation between RVEs increases with increasing volume fraction, decreasing model size and decreasing minimum imposed distance between fibers. For $V_f = 0.4$ and $p \leq 0.01$, convergence is only observed with $\delta > 30$, and nevertheless with significant variations between different RVEs.

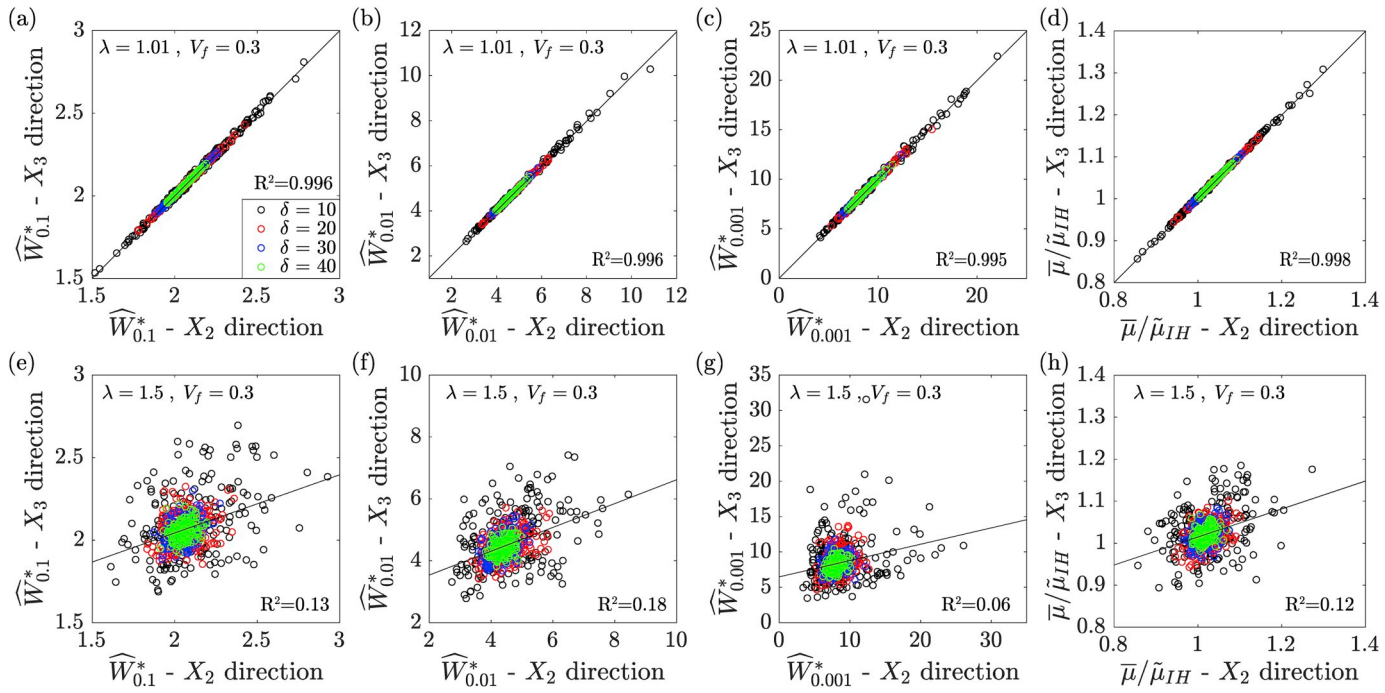

Fig. 8. Correlation of local strain energy density levels, $\widehat{W}^*_p$, under loading in the X_2 and X_3 directions, for RVEs with $V_f = 0.3$, and different sizes, δ. The applied stretches are $\lambda = 1.01$ (a–c) and $\lambda = 1.5$ (e–g). The correlation between the homogenized stiffness, $\overline{\mu}$, under the two loading directions and levels of applied stretch, is also shown (d,h). Each point corresponds to a different RVE realization. The lines correspond to a linear fit obtained using all values of δ; the values of R^2 are displayed for each fit.

We have also studied the correlation between strain energy in the matrix and the macroscopic response of the composite, characterized by the homogenized shear stiffness, for each of the RVEs analyzied. Obviously, there is a one-to-one relationship between stiffness and the *total* strain energy in the matrix, but this correlation decreases as increasingly smaller values of p are considered, implying that the presence of high strain and stress concentrations cannot be predicted by the macroscopic stiffness of a given RVE.

Remarkably, the distribution of strain energies and their correlation with the macroscopic response, are very similar in the case of linear and nonlinear applied stretches. Even so, the large strain response has shown two important effects fundamentally different from the response in the linear regime, and that should be taken into account.

First, despite showing similar overall statistical distributions of the strain energy, there is very little correlation between the response in the linear and nonlinear regimes for a given RVE, meaning that a given RVE could present low strain concentrations for small loading compared with nominal similar models, and high for large strains. In practice, this means that information of a given RVE in the linear regime cannot be used to predict its behavior in the non-linear regime.

Second, the response in the large deformation regime is strongly dependent on the loading direction, to the point that there is basically no correlation between the responses of the same RVE when the same stretch is applied in perpendicular directions, both as strain energy concentrations or macroscopic stiffness. If the RVE is not sufficiently large, the variations in the mechanical response between RVEs under the same loading direction are comparable to those of the same RVE under different loading directions. Studies performing statistical analysis on a large number of RVEs need to ensure that perceived differences between simulations are not an artifact of this anisotropy.

We hope the results presented in this study will contribute to the current efforts to develop a set of guidelines for RVE size and overall properties that is applicable to problems combining large deformations and failure mechanisms triggered by microscopic fields. In particular, the variations observed in the strain energy distributions in our results help rationalize the fact that RVEs sufficiently large to ensure convergence in the macroscopic response still show variations in damage initiation and progression [38,65,66]. It is expected that phenomena with strong dependence on very high values of the strain energy (corresponding to high values of p in the present study) will need to use large model sizes, as well as a large number of realizations of the RVE, in order to ensure that the results are statistically representative of the behavior of the real composite.

References

[1] Barbero EJ. Introduction to composite materials design. CRC press; 2017.
[2] Zhu J, Wei S, Ryu J, Guo Z. Strain-sensing elastomer/carbon nanofiber metacomposites. J Phys Chem C 2011;115(27):13215–22.
[3] López Jiménez F, Pellegrino S. Folding of fiber composites with a hyperelastic matrix. Int J Solids Struct 2012;49:395–407.
[4] Spackman CC, Frank CR, Picha KC, Samuel J. 3d printing of fiber-reinforced soft composites: process study and material characterization. J Manuf Process 2016;23:296–305.
[5] Agrawal A, Rahbar N, Calvert PD. Strong fiber-reinforced hydrogel. Acta Biomater 2013;9(2):5313–8.
[6] Ponte Castañeda P, Suquet P. Nonlinear composites. Adv Appl Mech 1998;34(998):171–302.
[7] Ponte Castañeda P. The effective mechanical properties of nonlinear isotropic composites. J Mech Phys Solids 1991;39:45–71.
[8] deBotton G. Transversely isotropic sequentially laminated composites in finite elasticity. J Mech Phys Solids 2005;53:1334–61.
[9] deBotton G, Hariton I, Socolsky E. Neo-hookean fiber-reinforced composites in finite elasticity. J Mech Phys Solids 2006;54:533–59.
[10] Lopez-Pamies O, Ponte Castañeda P. On the overall behavior, microstructure evolution, and macroscopic stability in reinforced rubbers at large deformations: II - application to cylindrical fibers. J Mech Phys Solids 2006;54:831–63.
[11] Agoras M, Lopez-Pamies O, Ponte Castañeda P. A general hyperelastic model for incompressible fiber-reinforcedelastomers. J Mech Phys Solids 2009;57:268–86.
[12] Lopez-Pamies O, Idiart MI. Fiber-reinforced hyperelastic solids: a realizable homogenization constitutive theory. J Eng Math 2010;68:57–83.
[13] deBotton G, Ponte Castañeda P. Elastoplastic constitutive relations for fiber-reinforced solids. Int J Solids Struct 1993;30(14):1865–90.
[14] Michel J, Moulinec H, Suquet P. Effective properties of composite materials with periodic microstructure: a computational approach. Comput Methods Appl Mech Eng 1999;172(1):109–43.

[15] Greco F, Luciano R. A theoretical and numerical stability analysis for composite micro-structures by using homogenization theory. Compos B Eng 2011;42(3):382–401.
[16] Kamiński M. Homogenization with uncertainty in Poisson ratio for polymers with rubber particles. Compos B Eng 2015;69:267–77.
[17] Catapano A, Jumel J. A numerical approach for determining the effective elastic symmetries of particulate-polymer composites. Compos B Eng 2015;78:227–43.
[18] Tsalis D, Chatzigeorgiou G, Charalambakis N. Homogenization of structures with generalized periodicity. Compos B Eng 2012;43(6):2495–512.
[19] Suquet P. Elements of homogenization for inelastic solid mechanics, vol. 272. Homogenization techniques for composite media; 1987. p. 193–278.
[20] Drugan W, Willis J. A micromechanics-based nonlocal constitutive equation and estimates of representative volume element size for elastic composites. J Mech Phys Solids 1996;44(4):497–524.
[21] Gusev AA. Representative volume element size for elastic composites: a numerical study. J Mech Phys Solids 1997;45(9):1449–59.
[22] Kanit T, Forest S, Galliet I, Mounoury V, Jeulin D. Determination of the size of the representative volume element for random composites: statistical and numerical approach. Int J Solids Struct 2003;40(13):3647–79.
[23] Sab K, Nedjar B. Periodization of random media and representative volume element size for linear composites. Compt Rendus Mec 2005;333(2):187–95.
[24] Khisaeva Z, Ostoja-Starzewski M. On the size of rve in finite elasticity of random composites. J Elast 2006;85(2):153–73.
[25] Trias D, Costa J, Turon A, Hurtado J. Determination of the critical size of a statistical representative volume element (srve) for carbon reinforced polymers. Acta Mater 2006;54(13):3471–84.
[26] M. Ostoja-Starzewski, X. Du, Z. Khisaeva, W. Li, Comparisons of the size of the representative volume element in elastic, plastic, thermoelastic, and permeable random microstructures, Int J Multiscale Comput Eng 5 (2).
[27] Gitman I, Askes H, Sluys L. Representative volume: existence and size determination. Eng Fract Mech 2007;74(16):2518–34.
[28] González C, LLorca J. Mechanical behavior of unidirectional fiber-reinforced polymers under transverse compression: microscopic mechanisms and modeling. Compos Sci Technol 2007;67(13):2795–806.
[29] Moraleda J, Segurado J, LLorca J. Finite deformation of incompressible fiber-reinforced elastomers: a computational micromechanics approach. J Mech Phys Solids 2009;57(9):1596–613.
[30] Heinrich C, Aldridge M, Wineman A, Kieffer J, Waas A, Shahwan K. The influence of the representative volume element (rve) size on the homogenized response of cured fiber composites. Model Simul Mater Sci Eng 2012;20(7):075007.
[31] Canal LP, González C, Molina-Aldareguía JM, Segurado J, LLorca J. Application of digital image correlation at the microscale in fiber-reinforced composites. Compos Appl Sci Manuf 2012;43(10):1630–8.
[32] Mehdikhani M, Aravand M, Sabuncuoglu B, Callens M, Lomov S, Gorbatikh L. Full-field strain measurements at the micro-scale in fiber-reinforced composites using digital image correlation. Compos Struct 2016;140:192–201.
[33] Alfaro MC, Suiker A, Verhoosel C, De Borst R. Numerical homogenization of cracking processes in thin fibre-epoxy layers. Eur J Mech A Solid 2010;29(2):119–31.
[34] Ismail Y, Yang D, Ye J. A dem model for visualising damage evolution and predicting failure envelope of composite laminae under biaxial loads. Compos B Eng 2016;102:9–28.
[35] González C, Segurado J, LLorca J. Numerical simulation of elasto-plastic deformation of composites: evolution of stress microfields and implications for homogenization models. J Mech Phys Solids 2004;52(7):1573–93.
[36] Nguyen VP, Lloberas-Valls O, Stroeven M, Sluys LJ. On the existence of representative volumes for softening quasi-brittle materials–a failure zone averaging scheme. Comput Methods Appl Mech Eng 2010;199(45–48):3028–38.
[37] Moraleda J, Segurado J, Llorca J. Effect of interface fracture on the tensile deformation of fiber-reinforced elastomers. Int J Solids Struct 2009;46(25–26):4287–97.
[38] López Jiménez F, Pellegrino S. Constitutive modeling of fiber composites with a soft hyperelastic matrix. Int J Solids Struct 2012;49:635–47.
[39] Estevez R, Maire E, Franciosi P, Wilkinson D. Effect of particle clustering on the strengthening versus damage rivalry in particulate reinforced elastic plastic materials: a 3-d analysis from a self-consistent modelling. Eur J Mech A Solid 1999;18(5):785–804.
[40] Bilger N, Auslender F, Bornert M, Michel J-C, Moulinec H, Suquet P, Zaoui A. Effect of a nonuniform distribution of voids on the plastic response of voided materials: a computational and statistical analysis. Int J Solids Struct 2005;42(2):517–38.
[41] Dautriat J, Bornert M, Gland N, Dimanov A, Raphanel J. Localized deformation induced by heterogeneities in porous carbonate analysed by multi-scale digital image correlation. Tectonophysics 2011;503(1–2):100–16.
[42] Trias D, Costa J, Mayugo J, Hurtado J. Random models versus periodic models for fibre reinforced composites. Comput Mater Sci 2006;38(2):316–24.
[43] Ghayoor H, Hoa S, Marsden C. A micromechanical study of stress concentrations in composites. Compos B Eng 2018;132:115–24.
[44] Maragoni L, Carraro P, Quaresimin M. Development, validation and analysis of an efficient micro-scale representative volume element for unidirectional composites. Compos Appl Sci Manuf 2018;110:268–83.
[45] Hill R. On constitutive macro-variables for heterogeneous solids at finite strain. Proc Roy Soc Lond A 1972;326(1565):131–47.
[46] Feder J. Random sequential adsorption. J Theor Biol 1980;87(2):237–54.
[47] Tanemura M. On random complete packing by discs. Ann Inst Stat Math 1979;31(1):351–65.
[48] Francis IV WH. Mechanics of post-microbuckled compliant-matrix composites. Ph. D. thesis. 2008. Citeseer.
[49] Pyrz R. Quantitative description of the microstructure of composites. part i: morphology of unidirectional composite systems. Compos Sci Technol 1994;50(2):197–208.
[50] Torquato S. Modeling of physical properties of composite materials. Int J Solids Struct 2000;37(1–2):411–22.
[51] Baxter SC, Graham LL. Characterization of random composites using moving-window technique. J Eng Mech 2000;126(4):389–97.
[52] Swaminathan S, Ghosh S, Pagano N. Statistically equivalent representative volume elements for unidirectional composite microstructures: Part i-without damage. J Compos Mater 2006;40(7):583–604.
[53] Vaughan T, McCarthy C. A combined experimental–numerical approach for generating statistically equivalent fibre distributions for high strength laminated composite materials. Compos Sci Technol 2010;70(2):291–7.
[54] Romanov V, Lomov SV, Swolfs Y, Orlova S, Gorbatikh L, Verpoest I. Statistical analysis of real and simulated fibre arrangements in unidirectional composites. Compos Sci Technol 2013;87:126–34.
[55] Wang W, Dai Y, Zhang C, Gao X, Zhao M. Micromechanical modeling of fiber-reinforced composites with statistically equivalent random fiber distribution. Materials 2016;9(8):624.
[56] Buryachenko V, Pagano N, Kim R, Spowart J. Quantitative description and numerical simulation of random microstructures of composites and their effective elastic moduli. Int J Solids Struct 2003;40(1):47–72.
[57] Liu KC, Ghoshal A. Validity of random microstructures simulation in fiber-reinforced composite materials. Compos B Eng 2014;57:56–70.
[58] Ogden R. Non-linear elastic deformations. Courier Corporation; 1997.
[59] López Jiménez F. Modeling of soft composites under three-dimensional loading. Compos B Eng 2014;59:173–80.
[60] Lopez-Pamies O. An exact result for the macroscopic response of particle-reinforced neo-hookean solids. J Appl Mech 2010;77(2):021016.
[61] López Jiménez F. On the isotropy of randomly generated representative volume elements for fiber-reinforced elastomers. Compos B Eng 2016;87:33–9.
[62] Grasset-Bourdel R, Alzina A, Tessier-Doyen N, Schmitt N, Huger M, Chotard T, Gruber D, Harmuth H. Optimisation of 3d rve for anisotropy index reduction in modelling thermoelastic properties of two-phase composites using a periodic homogenisation method. Comput Mater Sci 2011;50(11):3136–44.
[63] Salmi M, Auslender F, Bornert M, Fogli M. Various estimates of representative volume element sizes based on a statistical analysis of the apparent behavior of random linear composites. Compt Rendus Mec 2012;340(4–5):230–46.
[64] Savvas D, Stefanou G, Papadrakakis M. Determination of rve size for random composites with local volume fraction variation. Comput Methods Appl Mech Eng 2016;305:340–58.
[65] Elnekhaily SA, Talreja R. Damage initiation in unidirectional fiber composites with different degrees of nonuniform fiber distribution. Compos Sci Technol 2018;155:22–32.
[66] Waas AM, D'Mello RJ. The effects of rve size and fiber packing on the tensile and compressive transverse response of icme of fiber reinforced media. In: 2018 AIAA/ASCE/AHS/ASC structures, structural dynamics, and materials conference; 2018. p. 1900.